Methodological Advances on Pulse Measurement through Functional Imaging

Thirimachos Bourlai, Pradeep Buddharaju, Ioannis Pavlidis, and Barbara Bass

Introduction

The blood pressure and velocity rise rapidly as a result of the opening of the aortic valve in early systole. This spike in blood pressure and momentum travels the length of the aorta and is passed on to peripheral arteries such as the brachial, the carotid, and beyond. The thus formed pulse is an example of a traveling wave in a fluid medium that involves transport of mass and heat. The alteration of the electric field that moves the heart's muscle and the thermo-mechanical effects of pulse propagation in the vascular network creates opportunities for measurement across different modalities. The method that is considered to be the gold standard for pulse measurement is electrocardiography (ECG) [12]. It produces crisp results because it focuses on the source (heart). Other commonly used methods, such as piezoelectric probing [4], photoplethysmography [13] and Doppler ultrasound [9], focus on the vascular periphery. One main characteristic of all these methods is that they require contact with the subject. There are clinical applications, however, where a contact-free method is desirable. Such applications usually involve sustained physiological monitoring of patients who are in delicate state or form; examples range from sleep studies to neonatal monitoring.

The research presented in this article is in the context of stand-off physiological monitoring through passive imaging, a concept first proposed by Pavlidis et al. [17]. In this context, methods for measuring blood perfusion [16], vessel blood flow [10], breathing rate [15], and pulsation [6, 11, 19] have been developed.

Specifically, regarding pulsation, Chekmenev et al. [6] developed an interesting thermal imaging method that used wavelet analysis to quantify pulsation. Good performance results were reported on a dataset of eight subjects. The issues of tissue tracking and sensitivity analysis, however, were not adequately addressed.

T. Bourlai (✉), P. Buddharaju, and I. Pavlidis
Computational Physiology Lab, University of Houston, 4800 Calhoun Rd, Houston, TX, USA
e-mail: tbourlai@uh.edu

B. Bass
Department of Surgery, The Methodist Hospital, 7111 Fannin St, Houston, TX, USA

M. Garbey et al. (eds.), *Computational Surgery and Dual Training*,
DOI 10.1007/978-1-4419-1123-0_6,

Garbey et al. [11] and Sun et al. [19] developed different thermal imaging pulsation methods that used Fourier analysis. The dominant heart rate frequency was estimated by averaging the power spectra of each pixel in a preselected segment of a superficial vessel. Two variant methods were developed: the Along (ALM) [11] and the Across (ACM) [19]. The thermal imprint along (ALM) or across (ACM) the center line of a large superficial vessel was selected. Both methods were limited by the use of a non-optimal parameter set, the presence of tracking errors, and the lack of in-depth statistical analysis.

This paper addresses the limitations of previous contact-free approaches of pulse recovery and reports substantial methodological advances. The new pulse recovery thermal imaging (PRETI) method features parameter optimization for both the ALM and ACM models, which it uses within a fusion scheme. In this fusion scheme, there is a choice between three tissue tracking algorithms. These are the coalitional tracker, where a single tracking network is used, the tandem tracker, where two tracking networks are used in conjunction, and the micro-tracker, which features fine-tuning capability. The investigation reveals which measurement model (ALM or ACM) can pair with what motion tracking algorithm to offer a better trade-off between performance and computational complexity. All combinations are compared with the baseline (REF) pulse measurement methods [11, 19] in a set of experimental data drawn from 12 subjects, per approved protocol from the local Institutional Review Board (IRB).

The rest of the paper is organized as follows: section "Pulse Measurement Methodology" describes the new measurement methodology. Section "Experimental Setup" describes the experiments. Section "System Optimization" presents the optimization results. Finally, section "Conclusions" concludes the paper.

Pulse Measurement Methodology

PRETI is a fusion scheme that involves five steps: (1) Selection of Region of Interest (ROI); (2) Motion Tracking (tracking the ROI by using the single, sequential, or automatic tracker); (3) Blood Vessel Registration; (4) Noise Cleaning; and finally (5) Statistical Analysis. Figure 1 illustrates the steps of the new methodology that conclude with the computation of pulse. The computed pulse is compared against a "ground-truth" measurement provided by an ADInstruments piezoelectric device [1].

Selection of Region of Interest (ROI)

For a successful measurement of cardiac pulse via thermal imaging, selection, and knowledge of the anatomical region of interest is important. Stand-off pulse measurements are typically performed on the face, because it is easily accessible and

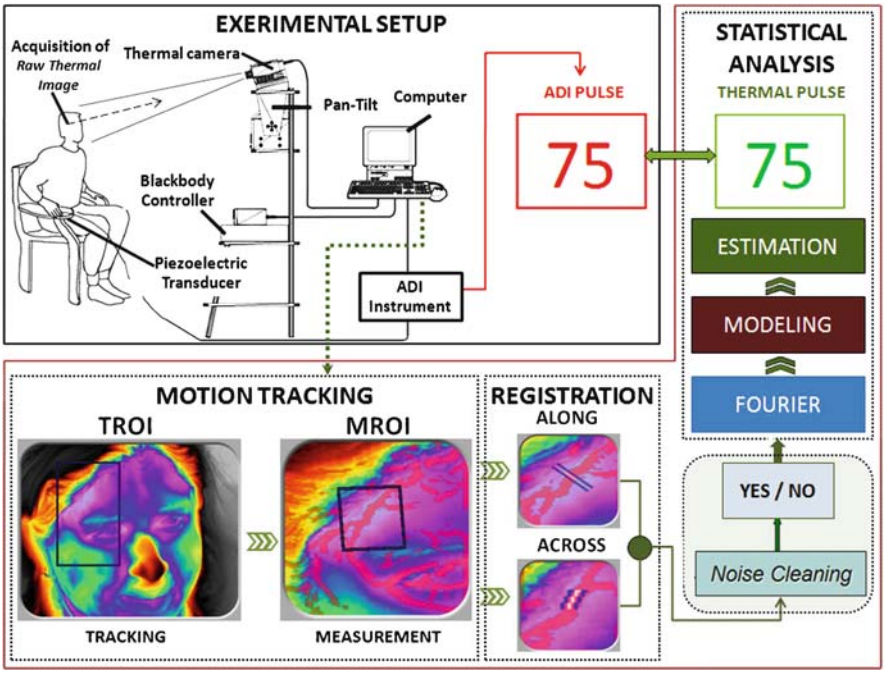

Fig. 1 Outline of the new pulse measurement methodology. The thermal imaging measurements are compared against "ground-truth" values provided by an ADInstruments piezoelectric device [1]

features major superficial vasculaturization. Periodic pulsation in facial vasculature results in localized skin temperature modulation through the mechanism of thermal diffusion [10].

Most of the facial vasculature is derived from the external carotid artery (ECA). The superficial temporal artery (STA) is a terminal branch of ECA. STA begins between the ear and the Temporo–Mandibular joint (TMJ) ascending upward and eventually splitting in the upper head area into the frontal and parietal branches (Fig. 2).

Pinar and Govsa [18] reported an excellent study on STA anatomy, its arterial branches, and their importance. For the purpose of thermal pulse measurement, STA is the region of choice because it is the most superficial vessel on the face and still has substantial size (2.73 ± 0.51 mm).

Motion Tracking

The proposed pulse measurement method is contact-free; hence, in the absence of good tracking, even the slightest movement by the subject will shift the ROI from its initial selection. PRETI employs three tracking algorithms, which are described

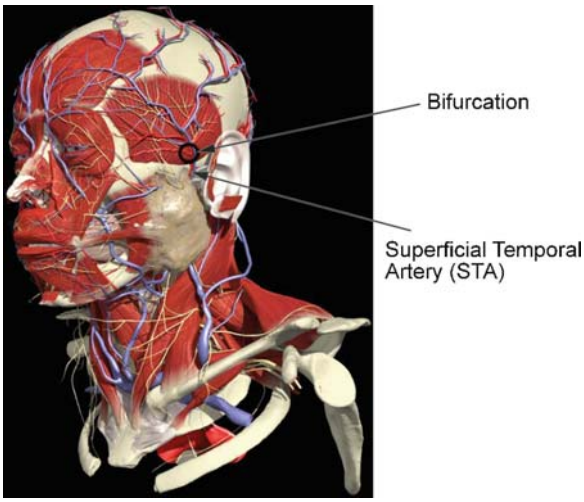

Fig. 2 Illustration of the superficial temporal artery (STA) and its bifurcation around the zygomatic arch – from Primal Pictures [14]

below, to compensate for motion and provide consistent ROI measurements over time. At this point, it is important to clarify that there are two types of ROI: The broader ROIs, which are the tissue areas upon which the trackers operate – these are the tracking ROIs (TROI). The smaller ROIs that are within the TROIs and atop the vessel's thermal imprint, where the measurement is performed – these are the measurement ROIs (MROI).

Coalitional Tracker

The coalitional tracking algorithm [7] optimizes collaboration among many simple particle-filter trackers, to achieve robustness and precision usually attainable only by model-based trackers. It was explicitly developed to support reasonable accuracy of vital sign measurements in thermal infrared, without resorting to modeling. Please note that modeling of highly dynamic imagery of physiological function is quite difficult. The coalitional tracker's performance deteriorates in the presence of out-of-plane rotations, which are due to pose changes of the subject's face. Figure 3 clearly illustrates such a case. The change in facial pose from time $t = 0$ (Fig. 3a) to time $t = 10$ sec (Fig. 3b) has caused the coalitional tracker to loosen its grip on TROI. At every point in time, the new TROI, as determined by the coalitional tracker, is used to produce the new MROI through a geometric transformation fixed during initialization. Thus, a small TROI error unavoidably translates to a small MROI error – typically a few pixels. Unfortunately, the thermal footprint of the vessel is also just a few pixels wide. Thus, even small tracking failures can throw MROI outside the vessel's thermal footprint and introduce substantial measurement errors (Fig. 3c, d).

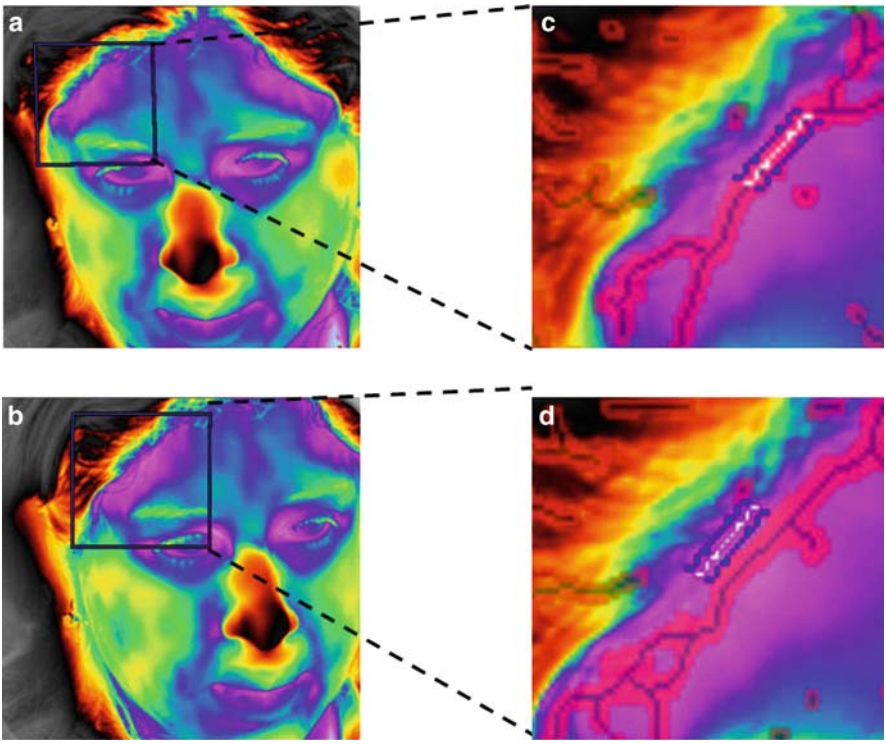

Fig. 3 Example of coalitional tracker performance. Thermal snapshots of the subject at time (**a**) $t = 0$ and (**b**) $t = 10$ sec with a coalitional tracker targeting the temporal area. Blow-ups of MROI at time (**c**) $t = 0$ and (**d**) $t = 10$ sec, where drift is evident. The tracker cannot cope effectively with pose changes

Tandem Tracker

The tandem tracking algorithm uses two coalitional trackers to overcome the errors introduced by a single coalitional tracker. The top coalitional tracker tracks a large TROI, which is centered in the general temporal area. At each point in time, this tracker provides cue about the initial position of another coalitional tracker, which tracks a smaller TROI centered on the temporal vessel. This "inside" coalitional tracker performs its own local tracking, using the cue from the top tracker as an initialization. Finally, the second tracker determines the position of the MROI, through a geometric transformation set at the beginning. Large coalitional trackers are prone to drift (and small inaccuracies), while small coalitional trackers to loss (and total failure). However, if small coalitional trackers do not get lost due to abrupt motion, they can afford much more accurate tracking than large ones. The tandem coalitional tracking scheme capitalizes upon these complementarities to deliver optimal performance (see Fig. 4).

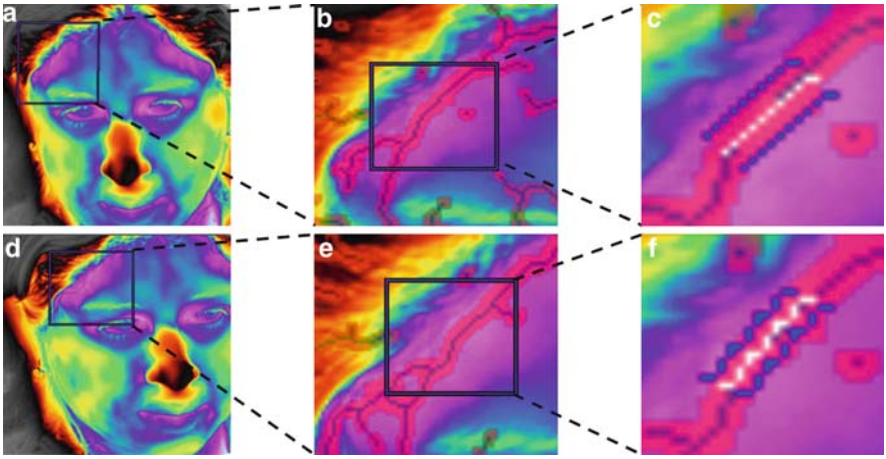

Fig. 4 Example of tandem tracker performance. Thermal snapshots of the subject with large TROI on the general temporal area, small TROI around the temporal vessel, and MROI on the thermal imprint of the temporal vessel at time $t = 0$ (**a**–**c**) and $t = 10$ sec (**d**–**f**)

Microtracker

The tandem tracker performs better than the single coalitional tracker at a premium computational cost. As a way to improve performance but at a more moderate computational cost, a third (and novel) micro-tracking algorithm was introduced. This algorithm, uses a single coalitional tracker in the general temporal area, which does not control the relative position of MROI through a rigid geometric transformation. Instead, MROI is localized at each point in time through a segmentation algorithm that operates in a smaller area around the temporal vessel. This is reminiscent of the inner TROI in the tandem tracker. The difference is that instead of secondary tracking, segmentation is taking place here. This segmentation fine-tunes the localization of the vessel's thermal imprint, stopping in essence the propagation of error from the top tracker (Fig. 5). The segmentation process involves the following steps:

Step 1: Within the inner ROI, perform top-hat segmentation to differentiate the vessels from the surrounding tissue [5]. The vessels' thermal imprints are usually at a gradient from the remaining region, because of convection from the flow of hot arterial blood.
Step 2: Thin the blood vessel network down to one pixel thickness [5].
Step 3: Find the largest vessel in case there are more than one within the inner region.
Step 4: Find the best fit for the points of the largest vessel through linear regression.

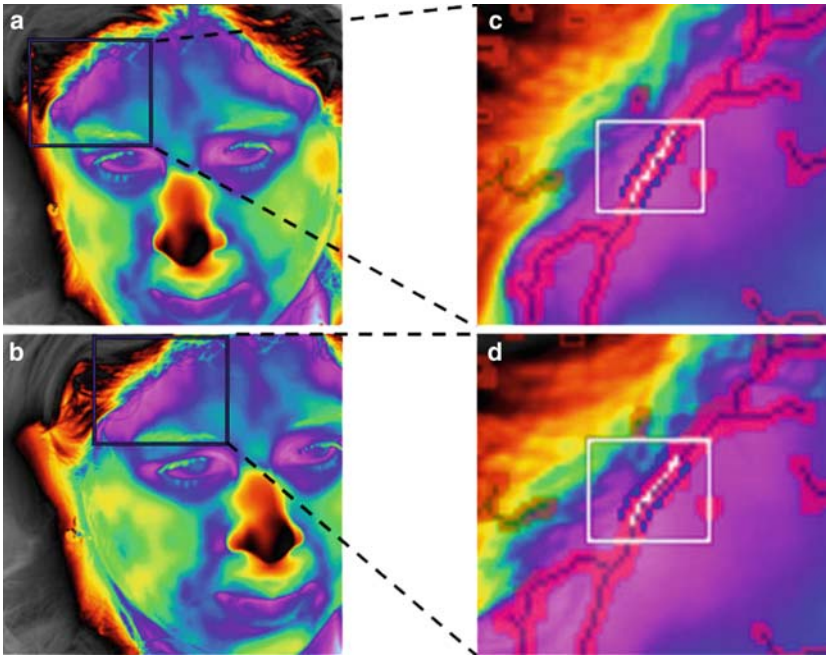

Fig. 5 Example of a microtracker performance. Thermal snapshots of the subject at time (**a**) $t = 0$ and (**b**) $t = 10$ sec with a coalitional tracker targeting the temporal area. Blow-ups of MROI and the inner region, where vessel segmentation is taking place, at time $t = 0$ and $t = 10$ sec

Blood Vessel Registration

The operator can select a thermal imprint along the center line of the STV or at 90° across it applying the ALM or ACM model respectively. The algorithm expands symmetrically into an elongated rectangle. The width of this rectangle depends on the width of the STV on the thermal imagery. For a subject imaged at 6 ft with a 50-mm lens, and when using the ALM model the rectangle's width is 3–7 pixels. By convention, in the ALM model, we place the x-axis of our coordinate system along the width and the y-axis along the length of the FSTA. We have the opposite coordinate system in the case of the ACM model. Note that the use of a rectangle in the case of ACM is a new approach investigated in our experiments. In the previous version of our ACM model, only a single pixel line of 90° across the vessel under study was considered.

1. *Tracking noise cleaning algorithm (TNCA)*. In the next stage, our newly developed TNCA process can be selected. It is a three-stage algorithm that assists our tracker in the selection of high confidence frames and by correcting the overestimated maximum pulse frequencies. Here follows a description of each stage:

(a) *Tracking confidence estimate (TCE)*. In order to achieve robust tracking, we have developed an algorithm that utilizes the final stage (target estimation) of the coalitional tracking process to decide whether a frame should be included in the pulse measurements or not. During target estimation, the winning coalition is produced by using a weighted sum of 4 scores at time t: Template Match, Geometric Alignment, Inter-frame projection agreement; and Inter-frame membership retention [7]. Confidence is the average template matching score (a number between [0, 1]) of all the trackers in the winning coalition. This score is computed frame by frame and rewards trackers that maintain consistent imaging content. The decision to include the frame at time t to the pulse measurement estimation process is based on a 70% confidence threshold. An example case is presented in Fig. 6.

(b) *Temperature thermal imprint estimate (TTIE)*. TTIE further assists the tracker to select frames where the segmented thermal imprints of the STV are of high quality. The thermal imprint at frame $t-1$ (TIF_{t-1}) is compared with the current thermal imprint at frame t (TIF_t). The comparison is based on the complement of the absolute normalized difference (CAND)$(1-\mathrm{ABS}(\mathrm{TIF}_t-\mathrm{TIF}_{t-1})/\mathrm{TIF}_{t-1})$, which is the absolute difference between the TIF_t and TIF_1 measurement normalized against the TIF_{t-1} and subtracted from unity. This gives a weighted indication of how close the TIF_1 measurement is to the TIF_{t-1} measurement in each case. Again, the decision

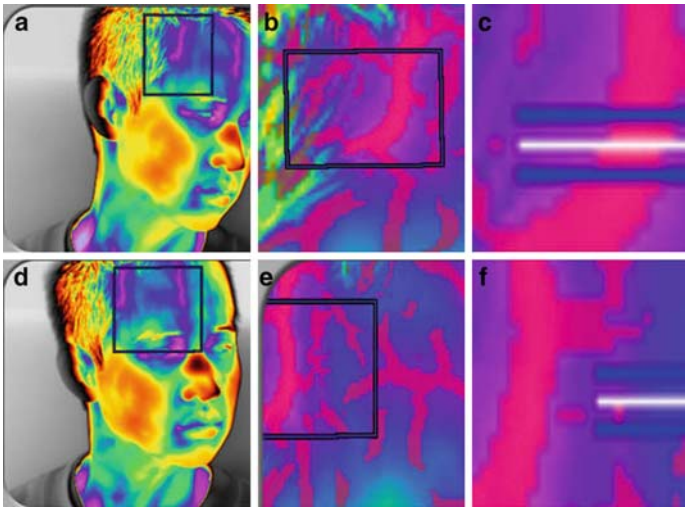

Fig. 6 Example cases of using the tracking confidence (TCE) and temperature thermal imprint estimate (TTIE) noise cleaning steps. (**a**) We can see the TROI where the tracker is having an 80% confidence, the resulting MROI at (**b**), and STV registration at (**c**) where the TTIE is 95%. (**d**) The tracking ROI where the tracker is having a 55% confidence, the resulting measurement ROI at (**e**), and frontal STV registration at (**f**) where the TTIE is 18%. In the (**d**), (**e**), and (**f**) cases the associated frame is rejected

to include the current frame to the pulse measurement estimation process is based on a 95% confidence threshold. Example cases where the TTIE is 95% vs. 18% are presented in Fig. 6c, f, respectively.

(c) *Peak correction*. Our experiments are set up in a quiet indoor environment and we test healthy subjects who are relaxed during the recording. Under these conditions, it is reasonable to assume that their pulse should range between 40 and 100 beats per minute (bmp). Therefore, we can facilitate pulse recovery by removing signals with frequency lower than 0.67 Hz (40 bmp) and higher than 1.67 Hz (100 bmp). This pulse range is selected by setting the low/high Pulse values in the common parameters section of the UI. However, there is still a possibility to overestimate/underestimate the maximum frequencies computed during pulse estimation. These can be triggered by a low/high estimation of the camera frame rate that affects the conversion of the pulse frequency from BPM to Hz (see (1)).

$$\text{Low/High rate} = \frac{\text{Low/High Pulse(BPM)} \times \text{TimeWindow}}{\text{Sec\_Per\_Min} \times \text{FrameRate}} \text{(Hz)} \quad (1)$$

Even though it is computed to be on average 30 frames per second (fps), it may go even below 20 fps or even above 45 fps. Thus, we may recover a sudden and very high/low pulse (e.g. 120/30 bpm) of a normal subject with an average pulse of 70 bpm. We know that in long observation periods the pulse frequency is expected to dominate in the spectral domain since it is more consistent than white noise. Therefore, in such cases, the algorithm can replace the overestimated pulse or peak frequency with the dynamic mean pulse frequency (DMPF) (see step three of the ACM model in Appendix).

DMPF is initially computed over an extended period of time T ($T \geq 30$ s). In our new methodology and in order to achieve a better DMPF measurement, we keep updating the mean pulse measurement. The estimation starts from the beginning of the clip and can be updated after each time window of 2^N frames ($N \in [7, 11]$) or $4k$ s ($k \in [1, 5]$). A typical window selected by the user through the UI is 64 frames or ≈ 0.5 s.

An example case where the peak correction step is employed is presented in Fig. 7.

2. *Statistical analysis*. In this step, we apply a Fourier-based method on the tracked ROI of the STV. It is applied in a novel manner to capitalize upon the pulse propagation effect and extract the dominant pulse frequency. Two models are used, the ALM and ACM when we select to operate either along or across the STV. By operating on the frequency domain and combining appropriately the power spectra of the time evolution signal of the temperature profiles, the signal can be reinforced. Thus, in the next stage, the adaptive estimation filtering (AEF) is employed in the same manner after either the ALM or the ACM modeling. AEF convolves the FFT outcome with a normalized historic power spectrum. In the last step, the cardiac pulse is computed by recovering the highest energy content of the filtered power spectrum.

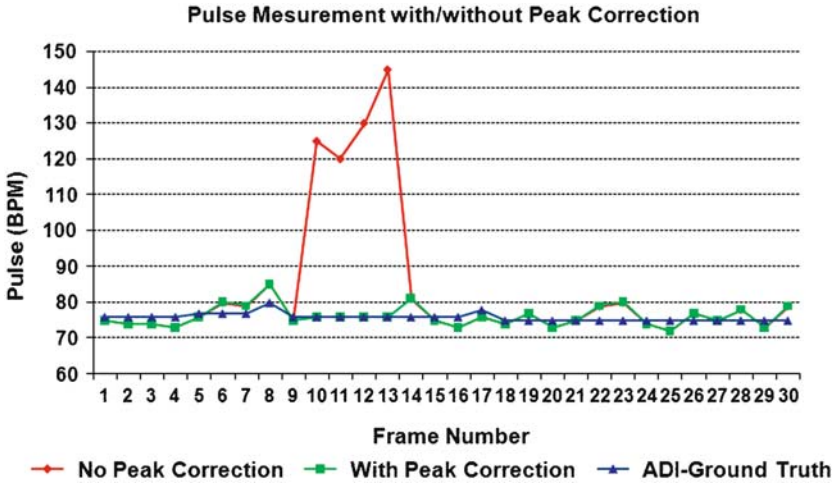

Fig. 7 Peak Correction example case. The algorithm can pick up wrong estimations of the thermal pulse at time t and correct them with the latest mean pulse update

A brief description of the ALM, ACM and AEF can be found in the Appendix. More details can be found on [11, 19].

Experimental Setup

A high-quality TI system has been designed for data collection that can obtain highly accurate measurements. The centerpiece of the system is an MWIR camera [2] with 50-mm lens. The lenses allow focusing on parts of the subject with rich superficial vasculature (e.g. face) at distances between 3 and 10 ft. The camera is capable of capturing 30 fps in a full spatial resolution of 640 × 480 pixels. The camera is placed atop a pan-tilt device to allow flexible positioning. We also use a differential blackbody as a calibrating device. The temperature resolution of the blackbody matches that of the thermal camera. To achieve maximum portability, all the aforementioned hardware components are placed in a cart and communicate with a powerful workstation.

Data collection is performed using healthy subjects. Subjects suffering from neuropathies, micro or macroangiopathy, as well as strong smokers have been excluded. Before data collection the subjects are briefed, and after that they signed a consent document. During data collection, each subject is placed about 6 ft away from the TI system. Then, as reported in section "Pulse Measurement Methodology," the TI measurements computed by our system are compared with the GT measurements. These are reported by the piezoelectric device. The MLT 1010 piezoelectric pulse transducer used is wired to the subject's index finger tip. Our pulse measurement experimental setup can be viewed in Fig. 1.

System Optimization

The optimization framework of the PRETI system in terms of performance and computational cost is quite complex. Global optimization requires an exhaustive evaluation of an uncountable number. Hence, in practice, only partial optimization is feasible with many parameters taking default values after an efficient parameter selection process. The main design issues are to fine-tune the harmonic analysis of the signals through parameter optimization of the baseline models, and then to improve the quality of the extracted physiological signals through sophisticated tracking and a noise reduction algorithm.

To evaluate the performance of our PRETI system, we employ three optimality criteria. The first and most important criterion is the Paired Student's t test (PSTT), a statistical hypothesis test that is used to compare two sets of quantitative data (in our case ground truth pulse and pulse estimation data). Please note that in [20] we have also used the Wilcoxon signed-rank test, as an alternative to the paired Student's t-test since the pulse measurements cannot be assumed to be normally distributed. However, the trend of the results did not change. Here we will report only the t-test results. We also calculate the cumulative sums (CUSUM) between the instantaneous pulse measurements and their corresponding ground-truth ones. In (2), we can see how the cumulative percentage error for subject i is computed.

$$E^i_{\text{cum}} = \frac{1}{T}\sum_{t=1}^{T}\frac{\left|S^i_{\text{T}}(t) - S^i_{\text{G}}(t)\right|}{S^i_{\text{G}}(t)} \tag{2}$$

Finally, we compute the normalized mean pulse difference (NMPD) which is based on the CAND of the mean pulse against the mean ground-truth measurements over the whole thermal clip (see (3)).

$$\text{NMPD} = 1 - \frac{\left|\overline{S}_{\text{T}} - \overline{S}_{\text{G}}\right|}{\overline{S}_{\text{G}}} \tag{3}$$

We tested our approach on 12 subjects (6 male/female) with ages in the range of 24–55 years old. The description of the parameter selection process follows.

Parameter Selection

The two main goals of this investigation are first to find the most efficient parameter set in terms of performance for each model and for all subjects. Then we prove that the application of those sets in combination with the use of the TNCA algorithm provide an additional performance advantage. Based on previous studies and the physiology of the vessels of the subjects under study, the baseline system (REF) involves both the ALM and ACM models and the fixed parameters are the length

(L) of the thermal imprint (7–10 pixels), the pulse range (40–100 bpm), and the time window (512 frames). In the REF system, there is no TNCA algorithm employed.

In this study for both models, we keep the length (L) of the thermal imprint and the pulse range that we restrict our investigation fixed as before. We investigate further into the importance of the width (W) of the thermal imprint, and the time window (frame range) of the history data. What follows is the investigation performed to identify the optimum parameter set per model in terms of performance.

- *ALM*. In the case of the ALM model, the values of W investigated are extended from 1 to 11 pixels in six steps $(1, 3, 5, \ldots, 11)$. The choice of these prime numbers guarantees that the central line selected by the operator is always in the middle on the vessel and the additional pixel lines are to the right and left of it. Also this range is practically selected so that any vessel width in the forehead of our 12 subjects is included within the MROI Fig. 8.
- *ACM*. In the case of the ACM model, the range of W is extended from 1 to 13 pixels in seven steps $(1, 3, 5, \ldots, 13)$ as shown in Fig. 9. Some additional parameters that are investigated are the quadratic interpolation (to apply or not and how many times) as well as the mean and variance of the normal distribution $N(\mu_p, \sigma_p^2)$.
- *Both models*. In both of our models, we extend the investigation of the time window from 128 and up to 2,048 frames (2^N frames for $N \in [7, 11]$) and we include the use of the TNCA algorithm and its associated parameters.

In Table 1, we present the parameters used before and after optimization.

The results of applying the optimum parameters in the REF system are presented in Table 2 where we can compare the performance of the baseline system with the optimized one, with and without employing the TNCA algorithm. Note also that

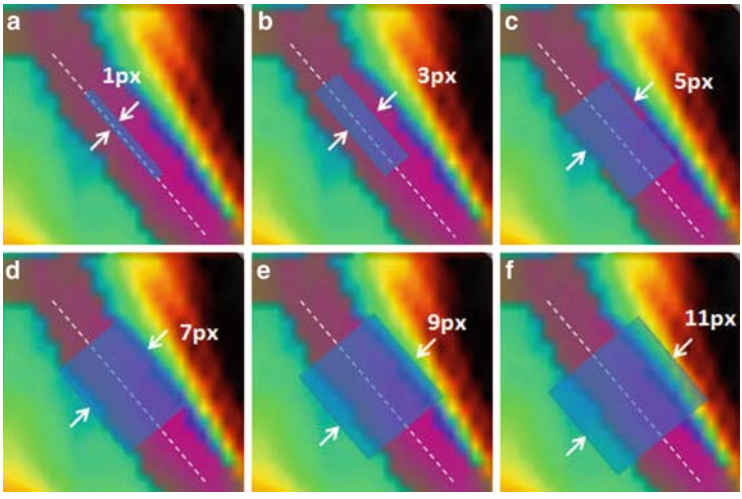

Fig. 8 ALM : Example case where the vessel width is 7 pixels. We can see how the ALM algorithm performs when we select different rectangles along the vessel orientation. The widths selected are (**a**) 1 px, (**b**) 3 px, (**c**) 5 px, (**d**) 7 px, (**e**) 9 px, and finally (**f**) 11 px

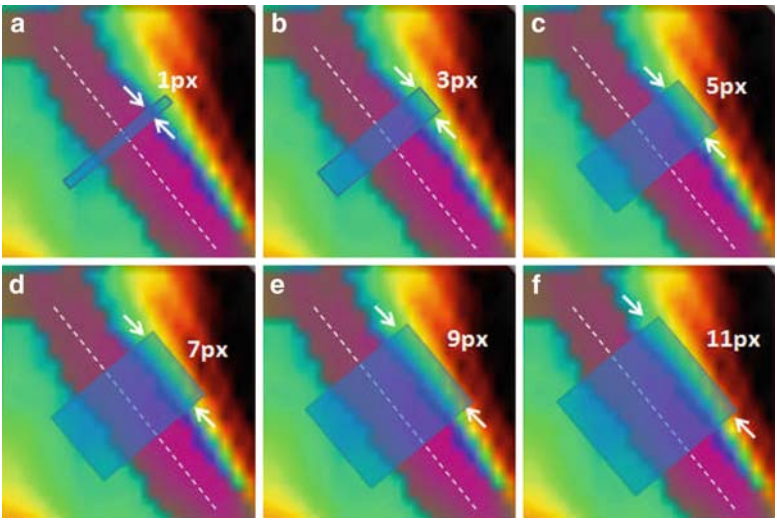

Fig. 9 ACM : Example case where the vessel width is 7 pixels. We can see how the ACM algorithm performs when we select different rectangles vertical to the vessel orientation. The widths selected are (**a**) 1 px, (**b**) 3 px, (**c**) 5 px, (**d**) 7 px, (**e**) 9 px, and finally (**f**) 11 px

Table 1 Parameters used before and after optimization

Models	Opt	TNCA	Length (px)	Width	TW	QI(ta)
ALM	No	No	7–10	3–7 px	512	–
	Yes	Yes	7–10	1 px	128	–
ACM	No	No	7–10	1 px	512	5
	Yes	Yes	7–10	7	2,048	1

Opt optimization, *TW* Time Window, and *QI(ta)* Quadratic interpolation (Times applied)

Table 2 Performance results before (REF) and after an efficient parameter selection and the use of the TNCA algorithm (OPT)

		REF			OPT		
MDL	TNCA	TT	CuSum	NMPD	TT	CuSum	NMPD
ALM	No	Fail	10.54	88.63	Fail	7.78	97.26
	Yes	–	–	–	Pass	6.89	97.57
ACM	No	Fail	10.14	94.56	Fail	8.15	98.50
	Yes	–	–	–	Pass	6.88	98.55

OPT Optimization, *REF* Baseline, *MDL* Model, *T T t* test

while the optimized parameter set was achieved for each subject, due to space constraints, here we present only the average performance results for all subjects.

Based on the above results, we can see that the efficient parameter selection achieved better performance results and that the use of the TNCA algorithm is the key for the statistical test to pass. Hence, in the next step, we select the optimum pa-

rameter set per model, we apply the TNCA algorithm, and then we investigate which motion tracking methodology we should follow to achieve maximum performance with the minimum computational cost. There are three alternative tracking optimization approaches that we can use, i.e. the SITA, the SETA and the AUTA as described at Section "Introduction." These are compared to the REF system. This study is analyzed in section "Motion Tracking."

Motion Tracking

After the optimum parameter selection for each thermal signal analysis model, our goal is to investigate various testing configurations. In our design strategy, we investigate the three alternative PRETIS tracking optimization approaches, the SITA, the SETA and the AUTA. By employing the optimum parameters and TNCA algorithm, we performed ten experiments per tracking approach for each subject. Then, the results are averaged and finally compared with the baseline approach. We use the same optimality criteria as described in the beginning of section "System Optimization," and at the same time, we compute the response time for each configuration. Both the performance as well as the response time results are presented below.

Performance Results

In Figs. 10–12, we illustrate the performance results for each subject when employing either the ALM or ACM model with the use of the optimum parameter set as well as the TNCA algorithm identified earlier. We can see the results after running each experiment 10 times for each of the SITA, SETA, or AUTA motion tracking approach. The criteria used are the CuSum and the NMPD as described in the beginning of section "System Optimization."

In Table 3, the final performance results are presented when averaging the above results for all subjects. We can see the benefits of optimization when comparing the REF and SITA approaches where only a single tracker was used before and after parameter optimization while using also the TNCA algorithm. Based on the t test criterion, it is clear that the SETA approach offers by far the best results. The CUSUM and NMPD criteria also support our selection. Finally, note that the AUTA approach did not perform as well as expected. Although very good results have been achieved, micro-tracking needs to be further optimized. This is planned to be part of our future work.

Response Time Results

The response time results are presented in Fig. 13 when using the REF system or any of the other three motion tracking optimization approaches. We are using blue color for the ALM model and red color for the ACM model. With blue is also indicated

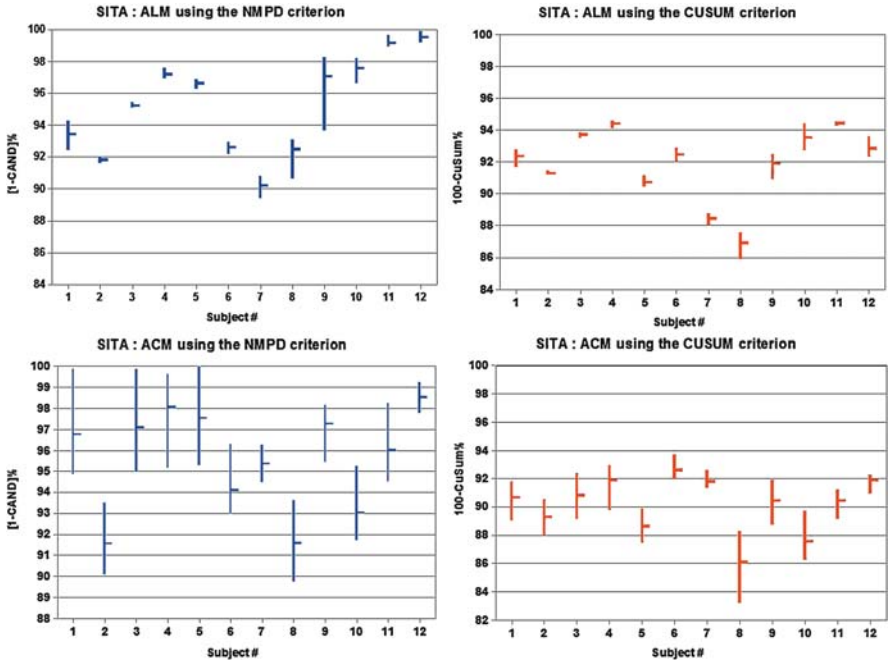

Fig. 10 ACM with SITA: Performance results when using the CuSum and the NMPD criteria. We perform ten experiments per parameter set and highlight the min, mean, and max values per subject and for each criterion employed

the average video time of all subjects that are processed in this study. In that way, we can see whether any of our approaches can process real-time all frames captured by the thermal camera.

In terms of time, the SITA approach when using the optimized ALM model gives the best time. However, in combination with our performance results, we highlight as our best option the SETA approach when using the optimized ALM model.

Conclusions

In this paper, we report substantial improvements in the design and methodology of a baseline pulse recovery thermal imaging system. The experimental results demonstrate that a proper parameter selection and the use of a TNCA algorithm have improved considerably the performance of our proposed PRETIS system when compared with the baseline one. TNCA in particular improves system performance up to 15.6% while imposing only a maximum of 3.98% increase in the computational complexity of the system.

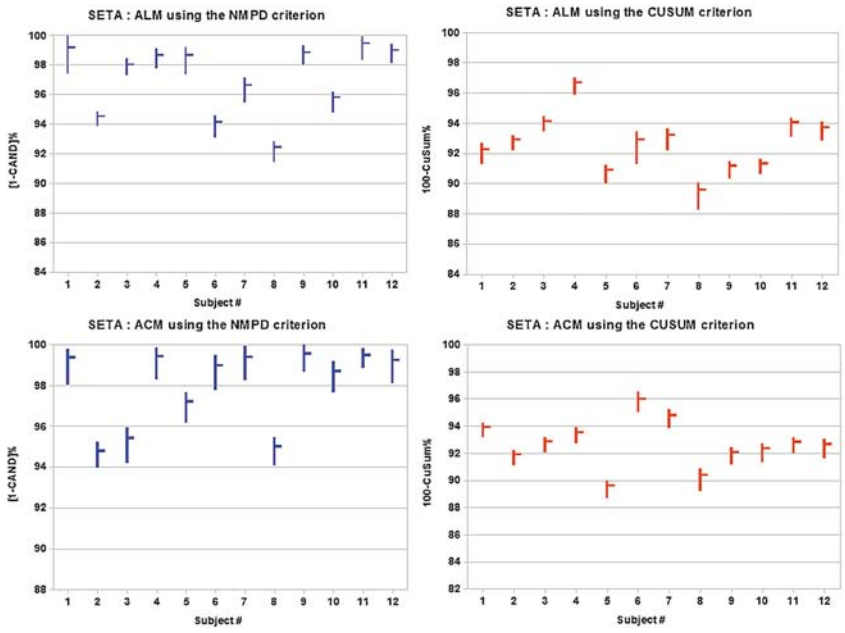

Fig. 11 ALM/ACM with SEQTP: Performance results when using the CuSum and the NMPD criteria. We perform ten experiments per parameter set and highlight the min, mean, and max values per subject and for each criterion employed

After an efficient parameter selection in either model of the baseline system, we compare three motion tracking methodologies in terms of system performance and response time. When using either model, the response time of SITA is the lowest one when compared with all other approaches and when using as a reference the baseline approach. However, it failed in almost 84% of the statistically significant tests. Even though SETA is 13% slower than SITA, it is still 11% faster than the baseline system when the ALM model is employed. SETA when using the ALM model proves to be the best overall solution also in terms of performance since it passes all statistically significant tests, achieving also the lowest CuSum error (7.26%) and the highest accuracy in terms of NMPD (97.11%). Similar results are achieved when using the SETA approach with the ACM model (almost all t tests passed, CuSum 7.27%, NMPD (98.04%). However, in this case, the response time is at least 4 times higher than when using the ALM model and thus it is considered to be our second best choice. Finally, even though AUTA was designed to further improve our pulse estimations by minimizing noise, it fails in about 80% of the statistically significant tests and thus its operation requires some further investigation.

Investigating different optimization strategies on a PRETI system is an interesting task. However, the conclusions of this work were drawn in the context of the our database. For future work, we plan to perform a new data collection process where a minimum of 30 subjects will participate. A new camera with a

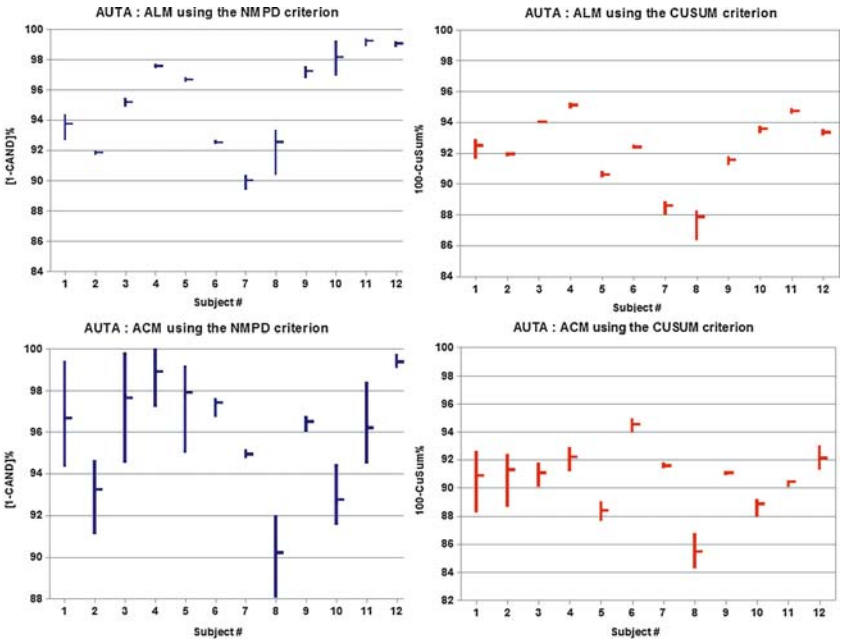

Fig. 12 ALM/ACM with AUTA: Performance results when using the CuSum and the NMPD criteria. We perform ten experiments per parameter set and highlight the min, mean, and max values per subject and for each criterion employed

Table 3 Final performance results when using the REF system and all our motion tracking approaches after optimization

Criteria	Method		REF	SITA	SETA	AUTA
T test	ALM		0	12	100	10
	ACM		0	17	97	20
CUSUM	ALM	Mean	10.56	8.11	7.26	7.82
	ACM	STD	10.14	9.84	7.27	9.35
	ALM	Mean	1.249	0.948	0.585	0.003
	ACM	STD	1.374	1.106	0.581	0.008
NMPD	ALM	Mean	88.63	95.24	97.11	95.32
	ACM	STD	94.56	95.23	98.04	95.04
	ALM	Mean	0.743	0.563	0.682	0.422
	ACM	STD	2.243	1.752	0.683	1.691

The mean values and standard deviation for all subjects are presented after running each experiment 10 times per subject
Opt Optimization, *REF* Baseline

better spatial resolution and a new protocol will be used that has been designed so that motion noise is minimized. Furthermore, we intend to optimize separately our new AUTA approach and to design a new theoretical framework that will improve system performance. We believe that our advanced research work will find

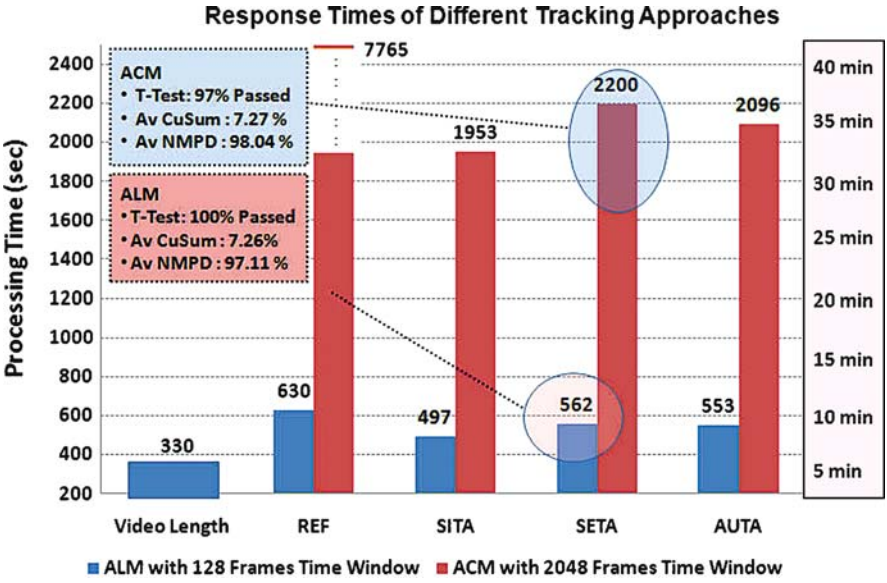

Fig. 13 Response time results when using the three motion tracking approaches. The best cases in terms of performance are also highlighted

great applications in the areas where the monitoring of heart rate through a passive sensing system is needed and in the cases where motion artifacts and poor subject cooperation are considered a serious problem.

Acknowledgements Research activity involving human subjects has been reviewed and approved by the University of Houston Committee for the Protection of Human Subjects. The authors would like to thank all the volunteer subjects who participated in their test population. They would also like to thank Dr. E. Glinert from the National Science Foundation (NSF) for his support and encouragement in this nascent technology effort. Equally, they would like to thank Dr. J. Levine from the Mayo Graduate School of Medicine for his valuable feedback.

Appendix

Description of the ALM Model: Here follows a brief description of the Along the Vessel Model:

- *In step one*, within the MROI, the operator selects manually or automatically a straight segment of 7–10 pixels (depending on the vessel selected) along the center line of the superficial blood vessel. The algorithm expands symmetrically into an elongated rectangle the width of which can be from 1 to 13 pixels (as opposed to 3–7 pixels used before). The width of this rectangle depends on the width of the vessel on the thermal imagery.

- *In step two*, we record the time evolution of the pixel matrix delineated by rectangle R for 2^N frames, where $N \in [7, 11]$ (only the use of $N = 9$ or 512 frames was reported in our previous studies. In this paper, we investigated all values of N). Thus, we produce a 3-D matrix $A(x, y, t)$, where x and y is the spatial extent of rectangle R and t is the timeline.
- *In step three* and in order to reduce the noise, we average the pixel temperatures along the x dimension.
- *In step four*, for each effective pixel on the measurement line, we obtain the time evolution signal of its temperature. We apply the FFT on each of these signals.
- *In step five*, we average all the power spectra computed in the previous step into a composite power spectrum.

Description of the ACM Model: Here follows a brief description of the Across the Vessel Model:

- *In step one*, the operator draws manually or automatically a line that traverses the cross section of the thermal imprint of the vessel (e.g., FSTA). The section spans between 1 and 15 pixels (as opposed to 3–7 pixels used before). The spatial resolution of the measurement line is increased by applying quadratic interpolation once (as opposed to 5 times used before) to minimize the computational complexity while achieving good performance. We model the cross section temperature function using the first five (5) cosine functions of the Fourier series.
- *In step two*, we compute the ridge and the boundary points at each frame. The first corresponds to the middle of the vessel's cross section, where the blood flow speed is maximal, while the second is recorded at the vessel's boundary where the minimum blood flow speed occurs. The time evolution of these points form the ridge and boundary temperature functions (R_{TF} and B_{TF}) respectively.
- *In step three*, we compute the static mean pulse frequency (SMPF). We apply the FFT on both R_{TF} and B_{TF} 1D signals and obtain their power spectrum (P_{r} and P_{b}). We model both power spectrum as a multi-normal distribution by applying a Parzen window method [8] and get the multi-normal distributions P'_{r} and P'_{b}. We multiply P'_{r} and P'_{b} to obtain the combined model spectrum P'_{rb}. Then, we find the frequency f_n for which P'_{rb} assumes its maximum amplitude. The f_n frequency is considered the SMPF of the subject during the time period of the first $T \geq 30$ s or $\approx$ 1,024 frames and it is represented as the normal distribution $N(\mu_{\mathrm{p}},\sigma^2_{\mathrm{p}})$ with mean $\mu_{\mathrm{p}}=f_{\mathrm{p}}$ and variance σ^2_{p}.

  In this paper, we go a step further and compute the dynamic MPF (DMPF). This is performed by updating the MPF for every 64 frames after the first 1,024 frames. We have also optimized the value of the variance to achieve better performance results.
- *In step four*, we compute the instantaneous pulse frequency (IPF). We apply exactly the same procedure that we described in step 3 for long observation periods ($T \geq 30$ s). Then, we can use either the SMPF or the DMPF computed to localize our attention in the IPF spectrum by multiplying $P_{\mathrm{rb}}\prime$ with $\mathrm{N}(\mu_{\mathrm{p}},\sigma^2_{\mathrm{p}})$ that is denoted as $P_{\mathrm{rb}}\prime\prime$. The tentative IPF is the frequency f_i for which the amplitude of the spectrum $P_{\mathrm{rb}}\prime\prime$ is maximum.

Adaptive Estimation Filter and Pulse Recovery: The instantaneous computation described by both ALM and ACM suffers by occasional thermo-regulatory vasodilation and noise despite the effective mechanisms built into both models. This problem has been addressed by building an estimation function that takes into account the current measurement as well as a series of past measurements. This idea is based on the adaptive line enhancement method reported in [3]. In our previous studies, we reported that the current power spectrum of the temperature signal is being computed over the previous 2^9=512 frames by applying the ALM or ACM models. Now, we investigate a frame range from 128 and up to 2,048 frames (2^N frames for $N \in [7, 11]$).

To compute the pulse frequency, first we convolve the current power spectrum computed by either model with a weighted average of the power spectra computed during the previous 60 frames. This is because at the average speed of 30 fps sustained by our system, there is at least one full pulse cycle contained within 60 frames even in extreme physiological scenarios. Then, we compute the historical frequency response (HFR) at a particular frequency. HFR is given as the summation of all the corresponding frequency responses for the spectra, normalized over the total sum of all the frequency responses for all the historical spectra. Finally, we convolve the HFR with the current power spectrum and we then designate as pulse the frequency that corresponds to the highest energy value of the filtered spectrum within the operational frequency band.

References

1. (2004) PowerLab Owner's Manual. ADInstruments Pty Ltd.
2. (2006) SC6000 Owner's Manual. FLIR Inc.
3. Akay M, Akay Y, Welkowitz W, Semmlow J, Kostis J (1992) Application of adaptive filters to noninvasive acoustical detection of coronary occlusions before and after angioplasty. IEEE Trans Biomed Eng 39(2):176–184
4. Aminian K, Thouvenin X, Robert P, Seydoux J, Girardier L (1992) A piezoelectric belt for cardiac pulse and respiration measurements on small mammals. In: Proceedings of the 14th annual international conference of the IEEE engineering in medicine and biology society, 2663–2664
5. Buddharaju P, Pavlidis I, Tsiamyrtzis P, Bazakos M (2007) Physiology-based face recognition in the thermal infrared spectrum. IEEE Trans Pattern Anal Mach Intell 29(4):613–626
6. Chekmenev S, Farag A, Essock E (2007) Thermal imaging of the superficial temporal artery: An arterial pulse recovery model. In: Proceedings of the IEEE computer society conference on computer vision and pattern recognition, Minneapolis, MN, 1–6
7. Dowdall J, Pavlidis I, Tsiamyrtzis P (2007) Coalitional tracking. Comput Vis Image Underst 106(2-3):205–219
8. Duda R, Hart P, Stork D (2001) Pattern classification. Wiley-Interscience, New York
9. Evans D, McDicken W (2000) Doppler ultrasound: physics, instrumentation and signal processing, 2nd edn. Wiley, Chichester
10. Garbey M, Merla A, Pavlidis I (2004) Estimation of blood flow speed and vessel location from thermal video. In: Proceedings of the IEEE computer society conference on computer vision and pattern recognition, vol 1. Washington, DC, pp 356–363
11. Garbey M, Sun N, Merla A, Pavlidis I (2007) Contact-free measurement of cardiac pulse based on the analysis of thermal imagery. IEEE Trans Biomed Eng 54(8):1418–1426

12. Guyton A (1991) Textbook of medical physiology, 8th edn. Philadelphia, PA, chap 3
13. Loukogeorgakis S, Dawson R, Phillips N, Martyn C, Greenwald S (2002) Validation of a device to measure arterial pulse wave velocity by a photoplethysmographic method. Physiol Meas 23:581–596
14. Moxham B, Kirsh C, Berkovitz B, Alusi G, Cheeseman T (2002) Interactive head and neck (CD-ROM). Primal Pictures, Castle Hill, NSW
15. Murthy R, Pavlidis I (2006) Noncontact measurement of breathing function. IEEE 25(3):57–67
16. Pavlidis I, Levine J (2001) Monitoring of periorbital blood flow rate through thermal image analysis and its application to polygraph testing. In: Proceedings of the 23rd annual international conference of the IEEE engineering in medicine and biology society, vol 3. Istanbul, Turkey, pp 2826–2829
17. Pavlidis I, Dowdall J, Sun N, Puri C, Fei J, Garbey M (2007) Interacting with human physiology. Comput Vis Image Underst 108(1-2):150–170
18. Pinar YA, Govsa F (2006) Anatomy of the superficial temporal artery and its branches: Its importance for surgery. Surg Radiol Anat 28:248–253
19. Sun N, Pavlidis I, Garbey M, Fei J (2006) Harvesting the thermal cardiac pulse signal. In: Medical image computing and computer-assisted intervention-MICCAI 2006, Lecture notes in computer science, vol 4191. Springer, Heidelberg, pp 569–576
20. Bourlai T, Buddharaju P, Pavlidis I, Bass B (Nov 2009) On Enhancing Cardiac Pulse Measurements Through Thermal Imaging. IEEE International Conference on Information Technology and Applications in Biomedicine, Larnaka, Cyprus